ADVANCED MATERIALS
www.advmat.de

Modular Aptamer Switches for the Continuous Optical Detection of Small-Molecule Analytes in Complex Media

*Amani A. Hariri, Alyssa P. Cartwright, Constantin Dory, Yasser Gidi, Steven Yee, Ian A. P. Thompson, Kaiyu X. Fu, Kiyoul Yang, Diana Wu, Nicolò Maganzini, Trevor Feagin, Brian E. Young, Behrad Habib Afshar, Michael Eisenstein, Michel J. F. Digonnet, Jelena Vuckovic, and H. Tom Soh**

Aptamers are a promising class of affinity reagents because signal transduction mechanisms can be built into the reagent, so that they can directly produce a physically measurable output signal upon target binding. However, endowing the signal transduction functionality into an aptamer remains a trial-and-error process that can compromise its affinity or specificity and typically requires knowledge of the ligand binding domain or its structure. In this work, a design architecture that can convert an existing aptamer into a "reversible aptamer switch" whose kinetic and thermodynamic properties can be tuned without a priori knowledge of the ligand binding domain or its structure is described. Finally, by combining these aptamer switches with evanescent-field-based optical detection hardware that minimizes sample autofluorescence, this study demonstrates the first optical biosensor system that can continuously measure multiple biomarkers (dopamine and cortisol) in complex samples (artificial cerebrospinal fluid and undiluted plasma) with second and subsecond-scale time responses at physiologically relevant concentration ranges.

1. Introduction

Aptamers have shown considerable promise as chemical recognition elements in biosensor systems because they can be chemically synthesized and can deliver high stability, sensitivity, and specificity.[1,2] However, since native aptamers do not inherently exhibit signaling activity upon target recognition, engineering approaches are needed to introduce signal transduction functionality so that they can generate a measurable output signal upon target binding.[3–5] A number of signaling modalities have been explored to date including electrochemical aptamer-based (E-AB) sensors, which measure changes in current that result from target-binding-induced conformational changes in redox-tagged aptamer molecules. E-AB sensors have repeatedly demonstrated the potential for continuous detection over extended periods of time in vivo with high specificity and stability.[1,2,6] However, the adaptation of existing aptamers for electrochemical platforms remains a bottleneck,[7] since aptamers identified through SELEX-based strategies will not necessarily undergo a meaningful conformational change upon target binding, and there is no guarantee that a promising aptamer can be readily engineered to generate an E-AB sensor that yields a sufficient signal response within the desired target concentration range. This limitation is one of the reasons why E-AB sensor implementation has been largely limited to a few target molecules such as doxorubicin,[8] kanamycin,[9] ATP,[10] and thrombin.[11]

Fluorescence-based optical readouts are of particular interest as they offer the capability to achieve single-photon sensitivity with appropriate detection hardware, can readily be multiplexed through fluorophores that emit at different wavelengths, and can accelerate the transition from aptamer selection to sensor development. Aptamer beacons[4,12–14] are a popular design strategy for fluorescence-based detection, in which an aptamer is labeled with a fluorophore and then combined with a separate, quencher-functionalized strand that directly competes with target binding, such that a fluorescence signal is only generated in response to target binding.[15] However, this method suffers from a major

A. A. Hariri, Y. Gidi, K. X. Fu, T. Feagin, B. E. Young, M. Eisenstein, H. T. Soh
Department of Radiology
Stanford University
Stanford, CA 94305, USA
E-mail: tsoh@stanford.edu

A. P. Cartwright, C. Dory, S. Yee, I. A. P. Thompson, K. X. Fu, K. Yang, N. Maganzini, B. H. Afshar, M. J. F. Digonnet, J. Vuckovic, H. T. Soh
Department of Electrical Engineering
Stanford University
Stanford, CA 94305, USA

D. Wu, H. T. Soh
Department of Bioengineering
Stanford University
Stanford, CA 94305, USA

H. T. Soh
Department of Chemical Engineering
Stanford University
Stanford, CA 94305, USA

The ORCID identification number(s) for the author(s) of this article can be found under https://doi.org/10.1002/adma.202304410

DOI: 10.1002/adma.202304410

drawback in the context of biosensor applications in that it cannot be used for continuous measurements, as the quenching sequence is unlikely to rehybridize once released. As an alternative, Tang et al. used a polyethylene glycol (PEG) moiety to couple aptamer sequences to a short complementary sequence, which were, respectively labeled with a fluorophore and quencher.[15–17] More recently, our lab devised another effective fluorescent sensor design based on intramolecular strand displacement (ISD) molecular switches, in which the complementary strand is physically coupled to the aptamer strand via a flexible linker. This strategy enables reversible switching and by modulating the lengths of the linker and the complementary region, one can achieve independent tuning of both the kinetics and thermodynamics of the resulting sensor.[18] However, both approaches face important limitations in that they require considerable trial and error optimization to achieve an ideal balance between minimizing the background signal and ensuring efficient target binding-induced displacement of the complementary displacement strand. Optimization typically requires detailed characterization of the aptamer's structure because postselection engineering of the aptamer often compromises its affinity or specificity. For these reasons, most aptamer switch designs to date have been prototyped with a handful of well-characterized aptamers for ATP,[13] cocaine,[19] and thrombin.[13] Multiple rational or semirational approaches have been developed to date to engineer aptamers to undergo a binding-induced conformational change, including enzymatic[5] and truncation approaches.[20] For newly discovered aptamers, however, these engineering processes remain challenging as it does not always yield a sensor with a sufficient signal response across the desired target concentration range. There is a need for a universal and systematic approach for reliably endowing switching functionality into aptamers to enable the efficient generation of biosensors for diverse molecular targets.

In this work, we describe a novel duplex-bubble switch (DBS) aptamer switch architecture, wherein any aptamer switch generated via Capture-SELEX[14,21,22] can be engineered in order to tune its kinetic and thermodynamic response without a priori knowledge of its structure or binding domain. Importantly, the DBS enables reversible switching, and we demonstrate that the architecture is suitable for use in continuous detection applications, achieving a rapid and reversible binding-induced fluorescent response at a time-scale of seconds even in complex biological matrices. We first show mathematically and experimentally that we can fine-tune the DBS design to precisely adjust the thermodynamics and kinetics of the resulting aptamer switches, both in solution and in a surface-coupled assay format. We then show that we can incorporate these DBS constructs onto a fiber-optic probe integrated with single-photon-counting hardware, exploiting a sensor design that allows us to achieve direct measurement of analytes in complex biological matrices while rejecting background autofluorescence from interferents and minimizing the impact of fouling. Specifically, we demonstrate continuous detection of dopamine in both buffer and artificial cerebrospinal fluid (aCSF) for more than a day with fast time resolution (<3 s) and a dynamic range spanning 500×10^{-9}–500×10^{-6} M. We subsequently developed a second, cortisol-specific DBS probe, achieving continuous cortisol detection in undiluted human plasma with nanomolar sensitivity and a dynamic range suitable for detecting physiologically relevant concentrations (200×10^{-9}–100×10^{-6} M) over the course of multiple hours in undiluted human plasma. The DBS design thus offers a generalizable approach to accelerate the transition from aptamer selection to sensor development, and to rapidly design aptamer-based sensors for the sensitive and specific continuous optical detection of diverse small-molecule analytes in a range of biomedical applications.

2. Results and Discussion

2.1. Duplex Bubble Switch Design and Modeling

The DBS is a double-stranded, multidomain fluorescent sensor (**Figure 1**), in which the aptamer is hybridized to a complementary displacement strand sequence. The aptamer is modified with an internal fluorophore, which is positioned to be adjacent to a quencher tag coupled to the 5′ terminus of the displacement strand. The 5′ end of the aptamer and the 3′ end of the displacement strand are each connected to complementary "anchor domains" via unpaired sequences that form the "bubble domain." This latter element acts as a flexible spacer to prevent conformational changes that would hinder aptamer target recognition and binding, while the anchor domain serves to tether the DBS to the sensor substrate.

The DBS can exist in three states: a quenched state in which the displacement strand is bound to the aptamer and thus suppresses the fluorophore emission, an unfolded state, and a target-bound state. In the absence of target, the quenched and unfolded states are in equilibrium, defined by the constant K_Q. Target binding shifts the equilibrium towards the target-bound complex, in which the quencher and fluorophore distance is increased, over the quenched state, thereby generating a fluorescence signal that increases with target concentration. The DBS design offers the advantage of enabling simple, rational design without requiring prior knowledge of the parent aptamer's secondary structure or binding site, thereby offering a more generalizable approach to the design of tunable aptamer switches. Indeed, any aptamer generated via Capture-SELEX[21,23,24] can be readily incorporated into a DBS construct, because the 5′ end of the aptamer domain is hybridized to its displacement strand via the same complementary sequence used during the original Capture-SELEX experiment, with no involvement from the target-binding domain of the aptamer.

We can also tune DBS thermodynamics and kinetics by modulating the hybridization of the aptamer to the displacement strand, enabling the sensor to achieve a dynamic range that is optimal for the desired target concentration while also undergoing switching at physiologically relevant concentrations.[3,18] The DBS design offers two parallel mechanisms for sensor tuning: decreasing the length of the bubble domain (L_{bubble}) is expected to reduce binding affinity (i.e., increase K_D^{eff}) while decreasing background, decreasing the peak signal, and increasing the overall rate of binding, whereas decreasing the length of the displacement strand (L_{DS}) reduces K_D^{eff} while increasing background signal, increasing the peak signal, and increasing the rate of binding. The mathematical model employed to predict the effects of tuning L_{bubble} and L_{DS} is derived and further discussed in Note S1 (Supporting Information).

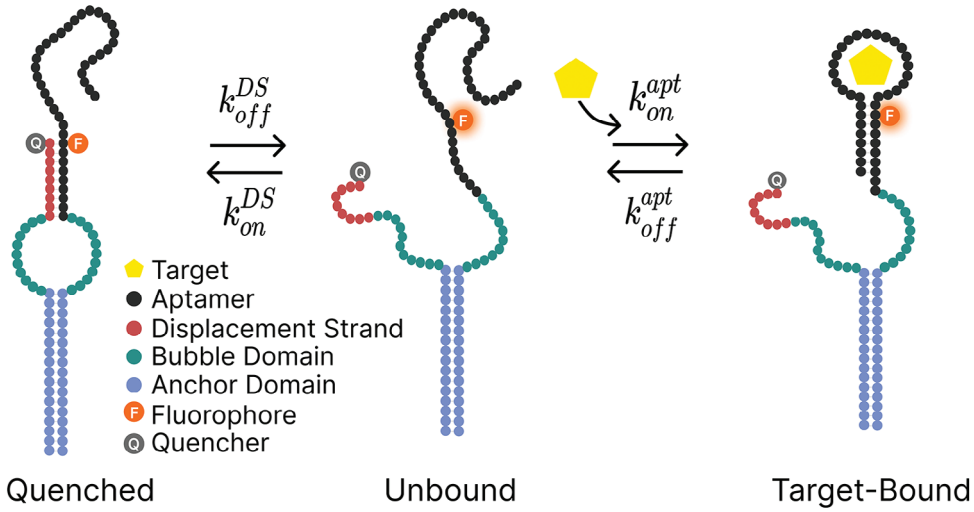

Figure 1. Schematic of the duplex bubble switch (DBS). The DBS converts an existing aptamer into a switch that produces a target-concentration-dependent signal based on alterations in the interaction of a fluorophore-quencher pair. In the absence of the aptamer target, the DBS exists in an equilibrium state between its quenched form (left), in which the quencher and fluorophore are in close proximity due to binding of the displacement strand to the aptamer, and the unbound state (middle), in which the two strands are dissociated. In the presence of the target, the system shifts to an equilibrium between the quenched state, unbound state, and the target-bound state (right), in which the fluorophore emission is greatly enhanced. This results in a target concentration-dependent signal increase.

2.2. Assessing the Affinity and Binding Response of a Dopamine DBS

As an initial demonstration for this work, we constructed a DBS based on an existing dopamine aptamer[23] (39 nt, $K_D = 150 \times 10^{-9}$ M) and tested these thermodynamic and kinetic tuning principles with our dopamine DBS in solution (Table S1, Supporting Information). We generated an array of DBS switches incorporating displacement strands with L_{DS} ranging from 7 to 12 nucleotides (nt) and L_{bubble} ranging from 12 to 52 nt and tested the dopamine-binding affinity of these constructs using a plate reader-based assay (see the Experimental Section). In order to increase the design space of DBS constructs, we also tested an aptamer sequence with a single mismatch introduced. We describe our switches using the nomenclature of L_{bubble}-L_{DS}, such that a construct with a 22-nt bubble and a 7-bp displacement strand is referred to as 22-7, and an asterisk (e.g., 22-7*) denotes use of the mismatched aptamer sequence. We selected a Cy3 fluorophore and an Iowa Black quencher to label the aptamer and displacement strands, respectively, in order to achieve long-term measurement with minimal fluorescence background or photobleaching. As expected, increasing L_{DS} on its own resulted in a lower background signal and lower apparent dopamine affinity. For instance, as we increased L_{DS} from 7 to 12 nt while maintaining $L_{bubble} = 22$, the majority of the corresponding aptamer switches exhibited lower sensitivity, with an increase in K_{Deff} from 37 to 170×10^{-6} M (**Figure 2**a and Figures S1 and S2, Supporting Information). In contrast, we generally observed greater

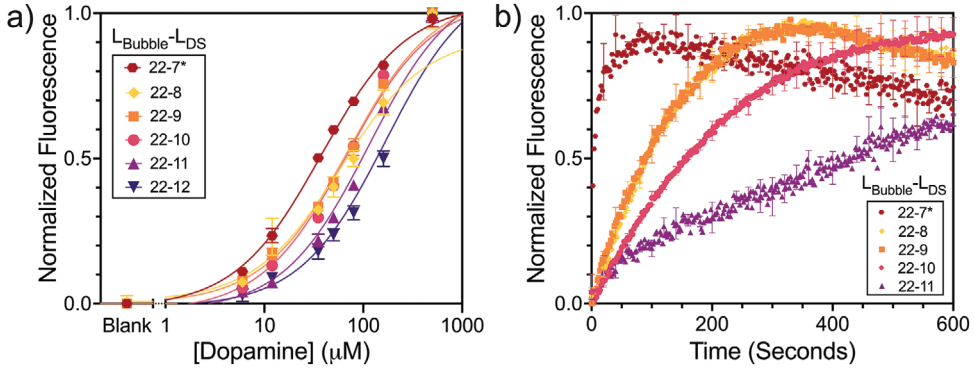

Figure 2. Tuning the performance of a dopamine DBS in solution. a) Changing the L_{DS} of our DBS from 7 to 12 bp while maintaining L_{bubble} at 22 nt shifts the binding curve to the right, indicating an increased K_D^{eff}. For ease of visualization, normalized data are presented here. b) Modulating temporal response to an injection of 50×10^{-6} M dopamine via tuning of L_{DS}. Increasing L_{DS} from 7 to 11 bp with a fixed L_{bubble} of 22 nt results in slower kinetics. Error bars are presented for every tenth data point for better visualization. Error bars represent the standard deviation of the average ($n = 3$). Raw thermodynamic plots for all DBS constructs are provided in Figures S1 and S2 (Supporting Information). Data normalization and fits are explained in the Experimental Section.

DBS sensitivity as L_{bubble} increased from 12 to 52 nt, with significant improvement in K_D^{eff} for every ten additional bases inserted while a constant L_{DS} was maintained. For example, while $L_{DS} = 10$, an increase in L_{bubble} from 12 to 52 nt resulted in a decrease of K_D^{eff} from 177 to 21 × 10^{-6} M. In addition to an increase in sensitivity, both background signal and peak signal increased with L_{bubble}, with peak signal approaching the theoretical maximum signal (Figure S3, Supporting Information). We note that while our experimental observations generally mirrored predicted trends from our model, we did observe several outliers, and this was likely due to unexpected secondary structure effects in certain constructs. These results highlight the importance of screening constructs prior to use (Figure S4 and Table S2, Supporting Information).

We subsequently tested our ability to tune the temporal response of our various constructs by adding 50 × 10^{-6} M dopamine to plate wells containing 250 × 10^{-9} M of each DBS construct and then observing the kinetics of the fluorescent response. Decreasing L_{bubble} with a constant L_{DS} did not meaningfully alter the kinetic response, but decreasing L_{DS} with a constant L_{bubble} (Figure S5 and Table S3, Supporting Information) resulted in significantly faster responses. We could dramatically increase temporal resolution (the switching time constant $\tau_{obs} = 1/k_{obs}$) by over 300-fold—from ≈17 min to less than 3 s—as we decreased L_{DS} from 11 to 7 nt in constructs with $L_{bubble} = 22$ (Figure 2b). For constructs with longer L_{DS}, we hypothesized that it should be possible to further improve their kinetic response by introducing mismatches into the aptamer-displacement strand duplex. Previous work has shown that such mismatches can enable more precise control over the binding curve and enhance the ability to increase kinetics without affecting affinity.[18,25] We therefore introduced single-base mismatches at different positions within the hairpin of the parent aptamer sequence and tested it with multiple constructs in which $L_{DS} = 11$ nt, a design that displayed very slow kinetics in the absence of mismatches (Figure S5, Supporting Information). In most cases, the introduction of mismatches dramatically increased the DBS association rate constant (τ_{obs}). For example, for construct 12-11, a mismatch at position 8 in the aptamer shifted k_{on} from ≈8 min to 35 s—a >12-fold improvement.

To test how well the DBS constructs perform when coupled to a solid support in the context of a biosensor system, we assessed the effect of surface anchoring on the affinity and binding kinetics of our 22-7* construct. We determined that 22-7* was the best candidate for further development, as it achieved the highest affinity of any of the DBS designs tested (K_D = 37 × 10^{-6} M) with a good dynamic range (1–100 × 10^{-6} M) while also undergoing switching at fast timescales (seconds). We biotinylated the 3′ end of the displacement strand-coupled anchor strand for surface attachment, and modified its 5′ end with Iowa Black quencher; the aptamer strand was internally modified with a Cy3 reporter. We immobilized this modified 22-7* construct onto a passivated, streptavidin-coated glass surface and used total internal reflection fluorescence (TIRF) microscopy to image dopamine binding with single-molecule resolution[26] (**Figure 3**a).

As we flowed a dopamine solution into a microchamber containing surface-immobilized aptamers, we were able to visualize in real-time the binding and release of individual dopamine molecules from the DBS as sharp increases and decreases in intensity (Figure 3b and Figure S6, Supporting Information). Our results confirmed that our DBS sensor can achieve robust dopamine detection when anchored to a solid substrate. Representative fluorescence intensity trajectories are shown in Figure 3c and Figure S6 (Supporting Information). By monitoring individual binding events in real time, we were able to calculate k_{on} via $1/\tau_{off} = k_{on}c$, where c is the dopamine concentration and τ_{off} is the mean dwell off-time. Similarly, the dissociation rate constant (k_{off}) can be calculated via $1/\tau_{on} = k_{off}$, where τ_{on} is the mean dwell on-time. In the absence of target, we observed monoexponential decays indicating long dwell off-time (183 s) and sporadic and short on-times (5.3 s). In contrast, the addition of target yielded monoexponential decays, with a marked decrease in dwell off-times (23.7 s) and an increase in dwell on-times (8.4 s) (Figure 3d). These equilibria in the absence and presence of dopamine allowed us to estimate a K_D^{eff} of 141 × 10^{-6} M ($K_D^{eff} = c\tau_{off}/\tau_{on}$), which is fourfold higher than the measurement we obtained in solution (K_D^{eff} = 37 × 10^{-6} M). These results indicated that surface coupling was influencing DBS affinity, possibly due to factors such as probe accessibility, the distance between probes, or probe–surface interactions.[27] Based on these results, we hypothesize that the k_{on} between target and aptamer would be minimally influenced by the displacement strand dissociation rate. However, once the target is bound, the association of the displacement strand could potentially destabilize the aptamer–target complex.

2.3. Development of a Near-Field Optical Probe System

To measure the signals from the DBS probes, we developed a fiber probe-based optical detection system that can achieve sensitive analyte detection directly in complex biological samples such as plasma without any sample preparation. The design of our optical probe system was guided by three major goals: 1) rejection of autofluorescence from the sample, 2) prevention of nonspecific binding and biofouling, and 3) maximizing sensitivity.

We designed our fiber probe to monitor DBS binding based on fluorophore excitation within an evanescent field. The evanescent field is generated when total internal reflection of light occurs within the core of the optical fiber, which is coated with a lower refractive index material. When the coating material is removed or greatly thinned and the fiber is inserted into an aqueous solution, the evanescent field is generated at the fiber–water interface (**Figure 4**a and Figure S7, Supporting Information). The field decays as it extends into the medium perpendicular to the fiber surface, such that fluorophores immediately adjacent to the surface (typically within 100–1000 nm)[18] will be excited by the evanescent wave; part of the resulting emitted fluorescence will in turn be coupled back into the fiber and can subsequently be measured. As such, DBS constructs coupled to the probe surface will generate measurable fluorescent signals in response to target binding that can be correlated to target concentration, whereas molecules in bulk solution located outside of the evanescent field will contribute very little to the measured signal, resulting in greatly reduced background noise.

In order to minimize biofouling, we functionalized the fiber tip in a multistep process (see the Experimental Section). After cleaning with piranha, acetone, and water, the probes were

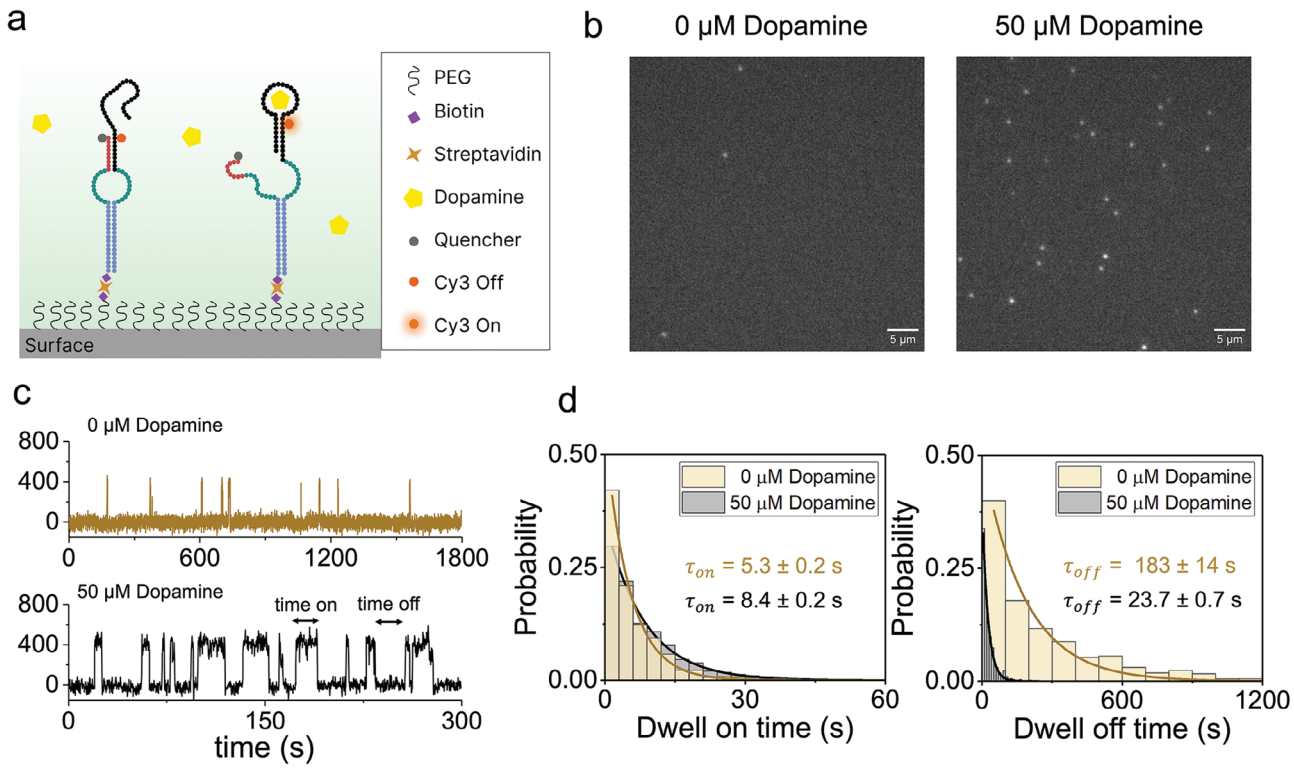

Figure 3. Characterization of surface-coupled dopamine DBS constructs. a) Schematic of DBS coupling to a streptavidin-modified glass substrate for analysis via total internal reflection fluorescence (TIRF) microscopy. b) The interaction of dopamine with surface-attached DBS probes yields temporal patterns of repeated on and off signals. Panels show single movie frames from a microscope field of view before (left) and after (right) dopamine addition (50×10^{-6} M), with bright puncta at locations where single fluorescent probes are bound. c) Representative intensity–time trajectories indicating on and off switching of single DBS constructs. d) Histograms of τ_{on} (left) and τ_{off} (right) for all intensity-versus-time trajectories observed within a single field of view in the presence or absence of dopamine with monoexponential fits.

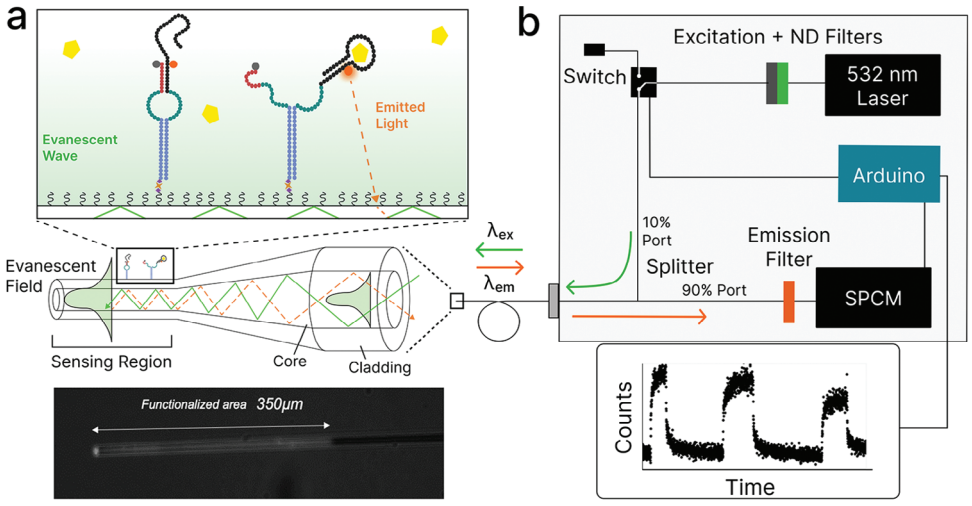

Figure 4. Near-field optical probe development and characterization. a) DBS constructs are immobilized onto a tapered optical fiber probe via biotin–avidin linkages to allow efficient near-field detection. Binding of target molecules to the DBS constructs is monitored in real time based on the excitation of fluorophore molecules within the evanescent field, where the emitted signal scales with incident power. Bottom panel shows fluorescence microscopy image of the tapered fiber tip functionalized with Cy3-labeled aptamers. b) A compact hardware system is used to excite DBS fluorescence and collect emitted fluorescence using a highly sensitive single-photon counting module (SPCM). Bottom panel shows an example of DBS signal over time as monitored in continuous mode.

functionalized with a mixture of unmodified and biotin-modified polyethylene glycol (PEG) polymer chains in order to insulate the probe against nonspecific binding while also enhancing the specific attachment of DBS molecules to the surface via biotin–avidin interactions.[28] We situated the probe within a microfluidic chamber (≈40 µL) by pressing a polycarbonate film with an adhesive gasket onto the PEG/PEG-biotin-coated fiber. Two silicone connectors were glued onto the predrilled holes of the film and served as inlet and outlet ports to manually dispense and wash out different solutions (Figure S8, Supporting Information). The fibers were then incubated with a neutravidin solution, which enabled direct coupling of the biotinylated DBS molecules to the biotin moieties at the end of the PEG chains (Figure 4a). Control experiments in which we incubated the functionalized probes with Cy3-labeled DNA strand in the absence of neutravidin ruled out any meaningful nonspecific binding of the aptamers to the sensor surface (Figure S7, Supporting Information), offering evidence that this design approach should generally help insulate against non-specific probe surface fouling.

Finally, to maximize our probe's sensitivity, we optimized the fiber design for high transmission of fluorescent signal and efficient evanescent coupling to the DBS probes. We selected a commercially available, graded-index, multimode silica optical fiber with a core diameter of 62.5 µm, low attenuation (≈3–5 dB km^{-1} at wavelengths of 650–850 nm), and low background fluorescence in the emission band of our dyes (Figure S9, Supporting Information). The chemical robustness and lack of oxidation of silica-based materials means that they remain stable in aqueous media for prolonged periods of time, and silica-based surfaces can easily be modified with passivation treatments that minimize biofouling in complex media.[29–32] To maximize the sensing volume—and therefore enhance the coupling between modes inside the fiber and the DBS construct—we tapered the base fiber down to a micrometer-scale tip (see the Experimental Section). Our fiber-tapering process was highly consistent, resulting in reproducible taper quality and dimensions and similar signals across several fiber probes (Signal CV = 0.10) (see Figure S10, Supporting Information). This optical fiber probe was then coupled to a sensitive single-photon counting module (SPCM) to achieve optimal detection performance.

The functionalized fiber was connected to an optoelectronic system (Figure 4b) that is designed to both excite the dye molecules on the DBS and collect the resulting fluorescent signal. The excitation-detection module contains the excitation laser (532 nm), with the appropriate laser line filters including variable neutral density filters to control incident power to the fiber probe. The laser light is coupled into a fiber and fiber switch, which allows for interval measurements and is controlled via a microcontroller (Arduino). This enables the laser to be switched between the sample fiber path (ON) and a dead-end port (OFF). The excitation laser is coupled to the functionalized fiber through the 10% port of a 90:10 fiber coupler. The emission light of the biosensor is collected with the same fiber and is coupled back into the excitation/detection box through the 90% port and then spectrally separated from the excitation laser via long-pass and notch filters. The emission signal from the fiber probe is then directed to the SPCM, which is interfaced to the Arduino to record detection events and monitor fluorescence intensity over time. Data acquisition was performed by a LabVIEW GUI with an integration time of 500 ms and 500 nW output laser power to minimize photobleaching (Figure S11, Supporting Information). The fluorescence response of the aptamer switch was defined as the fluorescence intensity of the target after subtracting the background from a blank fiber. By correlating this signal to analyte concentration, we could achieve precise real-time measurements of analyte concentration changes over time.

2.4. Continuous Detection of Dopamine in Buffer and Artificial Cerebrospinal Fluid

To characterize the sensitivity of the platform, we exposed our sensor to increasing and decreasing dopamine concentrations in buffer by intermittently injecting samples containing different analyte concentrations (0, 1, 8, 80, 200, or 800×10^{-6} м) into the chamber. Signal gain was calculated by background-correcting the fluorescence intensity and normalizing to the value observed at 0×10^{-6} м (see the Experimental Section). We observed a clear and proportional signal gain (**Figure 5**a and Figure S12, Supporting Information), ranging from 29% at 1×10^{-6} м to ≈2000% at 800×10^{-6} м, with an average CV of 0.15 at each concentration. We fitted the probe's signal gain to a Langmuir isotherm and obtained a K_D of 231×10^{-6} м, with a measured dynamic range of 1–800×10^{-6} м (Figure 5a and Table S4, Supporting Information). This limit of detection (LOD) is more than two orders of magnitude below the K_D of the DBS itself (231×10^{-6} м), demonstrating that even a DBS with modest affinity can achieve sensitive analyte detection in this probe design. By increasing the incident laser power—and thereby improving the signal-to-noise ratio—we could further lower the LOD from 1×10^{-6} to ≈200×10^{-9} м which falls within the previously reported physiological range[33–35] (Figure S13, Supporting Information). However, the gains from this strategy are mitigated by fluorophore saturation and photobleaching, which would limit the duration of measurements that can be collected in this fashion (Figure S11, Supporting Information). We next characterized the kinetics of the sensor upon exposing the probe to 8, 80, 200, and 800×10^{-6} м dopamine, and observed a rapid kinetic response, with $k_{on} = 138$ $м^{-1}$ s^{-1} and $k_{off} = 0.102$ s^{-1}. These measurements indicate that the probe reached 50% of its maximum signal within 7 s and then returned to 50% of baseline within 5.5 s (Figure S14 and Table S5, Supporting Information).

Our sensor also maintained high sensitivity over extended periods of time in buffer. We monitored the signal gain in response to multiple sets of ≥ 5 cycles of 8×10^{-6} м dopamine followed by buffer wash (100 s $cycle^{-1}$); we repeated this process at time intervals of 1, 16, 20, and 24 h after the start of the experiment (Figure 5b). Upon the first addition of dopamine at time zero, the sensor produced an average signal gain of 244%. After 16 h, the signal gain from the sensor decreased only slightly to 224%, and even after 24 h, we still observed an average signal gain of 271% over the course of a total of 40 dopamine-buffer cycles (average CV per time point = 0.035) (Figure 5b). Importantly, the sensor consistently returned to baseline with minimal drift (CV = 0.12) in buffer, even after 24 h. We also saw minimal inter-probe variability based on the signal gain produced after applying 8×10^{-6} м dopamine to six different fiber probes (CV = 0.11), as

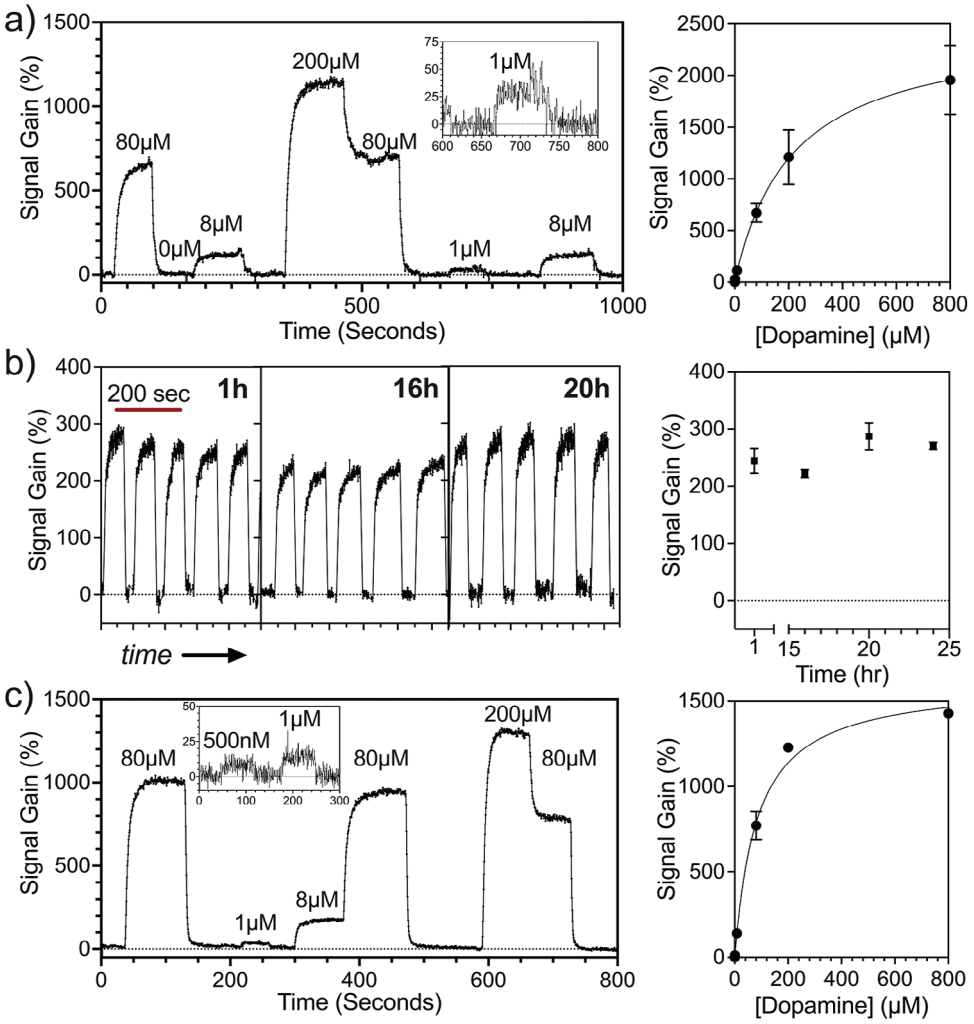

Figure 5. Real-time dopamine detection in buffer and artificial cerebrospinal fluid (aCSF). a) Continuous, real-time measurement of dopamine in buffer. Inset shows magnification of signal gain produced by 1×10^{-6} M dopamine. Right-hand panel shows a standard curve relating signal gain to dopamine concentration extracted from real-time data. Error bars represent the standard deviation over replicated measurements. Mean, CV, and number of replicates are reported in Table S4 (Supporting Information). b) The sensor maintained consistent response after multiple cycles of dopamine addition and wash after 1, 16, and 24 h. The plot on the right shows the average signal gain distribution of ten cycles for timepoints at 1, 16, 20, and 24 h. Error bars in the right-hand panel represent the standard deviation of the average at each timepoint ($n \geq 5$). Data fits and normalization are explained in the Experimental Section. c) Continuous, real-time measurement of dopamine spiked into aCSF. Right-hand panel shows magnification of signal gain from 500×10^{-9} and 1×10^{-6} M dopamine. Right-hand panel shows a standard curve relating signal gain to dopamine concentration extracted from real-time data. Error bars represent the standard deviation over replicated measurements. Mean, CV, and number of replicates are reported in Table S6 (Supporting Information).

well as minimal interprobe variability in standard curves across six different fibers (Figures S15 and S16, Supporting Information). In order to test our sensor under more physiologically relevant sensing conditions, we repeated the above experiments in aCSF, which contains salt and sugar and exhibits specific osmolarity and pH that mimic natural CSF in the brain (see the Experimental Section). Our sensor achieved essentially comparable performance in aCSF as we observed in buffer (Figure 5c and Table S6, Supporting Information), with a dynamic range of 500×10^{-9} to 800×10^{-6} M dopamine and an average CV per concentration of 0.04. We also observed temporal resolution in aCSF ($k_{on} = 149.4^{-1}$ s^{-1} and $k_{off} = 0.169$ s^{-1}) that was consistent with our results in buffer.

2.5. Continuous Detection of Cortisol in Undiluted Human Plasma

To demonstrate the generalizability of our platform, we developed a DBS-based sensor for the steroid hormone cortisol. Starting with a previously published cortisol aptamer[14] (51 nt, $K_D = 1 \times 10^{-6}$ M), we generated multiple DBS switches with variable L_{DS} and L_{bubble} (Table S1, Supporting Information) and tested their affinity in solution using a plate reader-based assay. Decreasing L_{bubble} from 32 to 22 nt while maintaining a constant L_{DS} of 8 nt improved the aptamer affinity by almost sevenfold from 97.46 to 14.24×10^{-6} M. In addition, as with the dopamine DBS, decreasing L_{DS} while maintaining a constant L_{bubble} resulted in

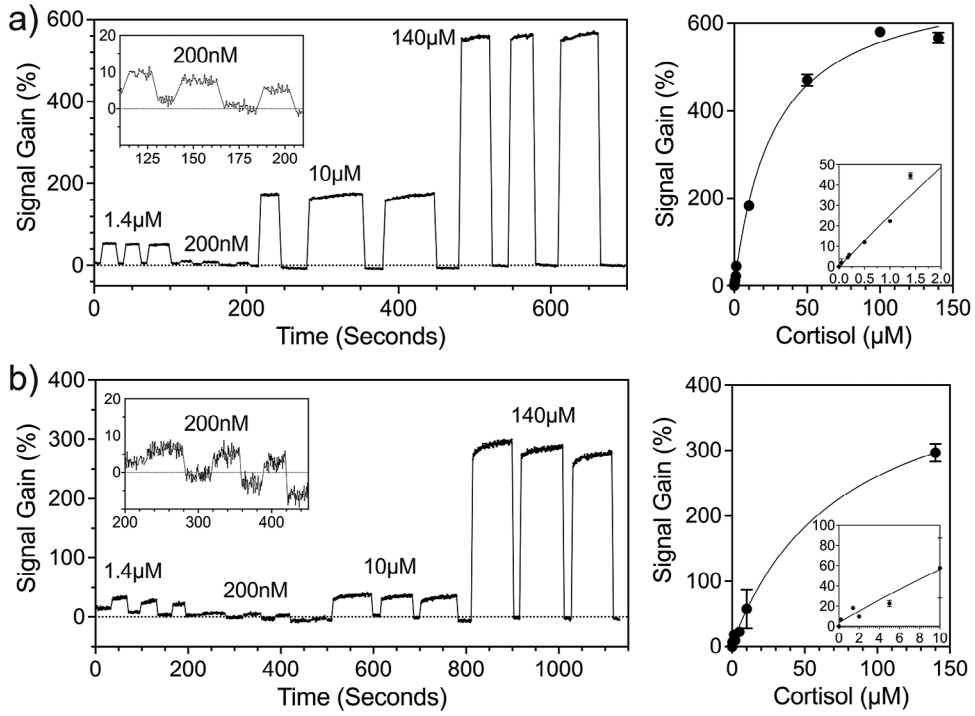

Figure 6. Cortisol detection in buffer and undiluted human plasma. Continuous, real-time measurement of cortisol in a) buffer and b) undiluted human plasma. Insets show magnification of signal gain at low concentrations, right-hand panels show standard curves, with linear ranges presented as insets. Error bars represent the standard deviation of the average ($n = 3$). Data fits and normalization are explained in the Experimental Section.

higher sensitivity, with a decrease in K_{Deff} from 97.46×10^{-6} M for 32-8 to 35.03×10^{-6} M for 32-7 (Figure S17 and Table S7, Supporting Information). We therefore selected 22-8 for coupling to our fiber probe, as this construct achieved a dynamic range (500×10^{-9} to 175×10^{-6} M) that fell closest to expected physiological concentrations ($55–690 \times 10^{-9}$ M).[36,37] After fabricating the fiber probe as described above, we exposed our sensor to varying cortisol concentrations in buffer (0×10^{-9}, 200×10^{-9}, 1.4×10^{-6}, 10×10^{-6}, and 140×10^{-6} M). Our sensor exhibited clear and proportional signal gain across this concentration range, from 5.9% at the LOD of 200×10^{-9} M to 567% at 140×10^{-6} M (**Figure 6**a). We observed minimal variance at each concentration tested (average CV = 0.012). This switch also produced a very rapid, subsecond kinetic response (Figure S18, Supporting Information). By increasing the incident laser power from 500nW to 5 μW and thereby improving the signal-to-noise ratio, we achieved a LOD of $\approx 50 \times 10^{-9}$ M (Figure S19, Supporting Information)—roughly three orders of magnitude below the K_D of the DBS ($\approx 14 \times 10^{-6}$ M) and at the lower bound of the physiological concentration range of this analyte.

Finally, we demonstrated that our sensor could achieve robust, continuous cortisol sensing in undiluted human plasma. We sequentially exposed the sensor to varying concentrations of cortisol spiked into plasma (0×10^{-6}, 200×10^{-9}, 1.4×10^{-6}, 10×10^{-6}, and 140×10^{-6} M) and observed close correlation in terms of signal gain (Figure 6b), ranging from 6.5% at 200×10^{-9} M to 296% at 140×10^{-6} M, with a similar LOD (200×10^{-9} M) compared to our buffer measurements. We also observed slightly higher variability in our replicate measurements for each concentration tested on the probe (average CV = 0.05). This increase in CV and decrease in signal gain (Table S6, Supporting Information) may be attributable to a number of reasons, including the fact that free cortisol is known to bind to the corticosteroid-binding proteins globulin and albumin in plasma, potentially resulting in depletion of the spiked-in cortisol in our experiments.[38] Nevertheless, these results clearly demonstrate that our DBS-coupled probes can achieve rapid, quantitative detection of protein analytes in complex, minimally processed samples, and highlight the generalizability of this approach.

3. Conclusion

We have demonstrated a generalizable strategy to convert an existing aptamer into a modular DBS architecture that is capable of continuous optical detection of small-molecule analytes in complex samples. These constructs can be assembled and fine-tuned to adjust the thermodynamics and kinetics of the resulting switches without prior knowledge of the aptamer's structure or binding domain. As proof of concept, we generated DBS-based sensors for two different analytes—dopamine and cortisol—in which we coupled our switch constructs to a surface-functionalized fiber-optic probe that can sensitively detect binding-induced fluorescent signals within an evanescent field, enabling us to minimize the confounding effects of background autofluorescence and surface fouling. Using this sensor design, we demonstrated that we could detect nanomolar concentrations of these two targets in both buffer and complex specimens such as aCSF or undiluted human plasma.

Furthermore, our probes could rapidly respond to both increases and decreases in analyte concentration with subsecond resolution, while demonstrating the potential to achieve robust performance over longer periods of use. We saw reasonably consistent signal gain with our dopamine measurements after more than 24 h in buffer (Figure 5b), and even with undiluted plasma, we were able to achieve stable performance over the course of multiple hours (Figure S20, Supporting Information). We generally observed excellent sensitivity with our sensors, achieving LODs that were typically several orders of magnitude lower than the K_D of the DBS component itself; this suggests that sensors based on even higher-affinity aptamers (e.g., low nanomolar K_D) should be able to monitor even lower-abundance analytes. And as demonstrated with both analytes, increased laser power can greatly improve the sensor's sensitivity at the cost of a shorter time window for detection due to heightened photobleaching. However, we did observe diminished cortisol sensitivity in plasma, and we believe this is principally attributable to the choice of target and the detrimental impact of cortisol-binding proteins present in the matrix.[38] As such, we can most likely improve our cortisol sensor's performance through the selection of an aptamer that can bind and measure both free and bound cortisol. Despite these limitations, our initial demonstration with cortisol in plasma hints at the potential clinical utility of this sensor design. The normal range of cortisol concentrations in plasma fluctuates from $136–690 \times 10^{-9}$ M in the morning to $55–386 \times 10^{-9}$ M in the evening,[36,37,39] but pathological states such as heart disease can give rise to considerably elevated levels of cortisol ($>690 \times 10^{-9}$ M).[39–41] Our proof-of-concept sensor could therefore be leveraged in biomedical applications focused on diagnosing and monitoring conditions associated with spikes or other irregularities in cortisol levels.

More generally, the observed limitations in sensor performance are fundamentally attributable to the limitations of the parent aptamers. Our fiber sensor has demonstrated the capacity to detect analyte concentrations that are 2–3 orders of magnitude below the K_D of the DBS construct. As described in Note S1 (Supporting Information), this latter value is bounded by the K_D of the parent aptamer, which is increased by the addition of the displacement strand and anchor strand. We therefore see considerable opportunities to select novel aptamers with K_D values closer to the range of physiological concentrations, and there are numerous examples of aptamers with baseline affinities in the nanomolar range.

Although we could achieve robust cortisol detection in human plasma for a few hours, the signal gain subsequently degraded over longer periods of time (Figure S20, Supporting Information). Our system is designed to counter the effects of biofouling, indicating that this may not be the primary source of this problem, but there are other factors that likely contribute to this degeneration over time. For example, the natural DNA-based DBS constructs may be susceptible to degradation in the complex plasma environment, and recent work has shown that the use of nuclease-resistant, chemically modified nucleobases can greatly enhance aptamer durability in such sample conditions.[42] Such modifications will be worth exploring in subsequent implementations of this sensor platform, and our future efforts will be focused on enhancing this system's performance in complex biosamples with the ultimate aim of achieving sensitive, long-term analyte detection in flowing blood and other clinically relevant sample matrices. We also see other opportunities to improve this technology. For one, the aptamer DBS switch design effort currently entails some degree of trial-and-error, in which multiple constructs are synthesized and evaluated. Our recent work on high-throughput screening methods[42,43] could broaden the scope of this process while also accelerating the identification of switch constructs that offer the best dynamic range and kinetics for a particular target in a given sample matrix. Despite the narrow range of constructs tested here, considerable further tuning of the DBS design is possible. L_{bubble} is only limited by the constraints of DNA synthesis, although increasing L_{bubble} has diminishing returns—each additional base has a smaller impact on both the thermodynamics and kinetics, as was demonstrated previously.[18] The displacement strand length is currently constrained by the length of the complementary hairpin integrated within the Capture-SELEX library design. For aptamers not selected through Capture-SELEX, the displacement strand could be as long as the aptamer itself—or even longer, if bulges were included—but this would result in a very high K_D^{eff}. Although the displacement strand could potentially be as short as 5 nt, a shorter displacement strand produces a very high background signal, and $L_{DS} < 5$ nt is not recommended without also incorporating hybridization-enhancing modified bases such as peptide nucleic acids or locked nucleic acids. Sensor performance could also be further enhanced by using alternative fluorophores that minimize the effects of photobleaching and photodegradation, or via the implementation of ratiometric-based fluorescence measurements such as Förster resonance energy transfer (FRET), which can contribute to greater sensitivity and minimal background and drift issues.

We believe that this approach has the potential to accelerate development of a diverse range of continuous biosensors for physiological monitoring and improved patient care. However, there are still multiple challenges associated with operation in live animals,[44] including signal degradation over time. Solutions such as membrane protection, nanoporous fibers, and hydrogels to shield the aptamers from proteins and cells present in the biofluid can be explored in future work. It should also be noted that although aptamer-based optical sensors are promising,[30,32] this modality is still in its infancy relative to other real-time sensing platforms such as E-AB sensors, which have demonstrated resilience in complex samples and in vivo applications.[7,8,45,46] However, electrochemical aptamer switches require a conformation change that brings the redox reporter closer to the electrode surface, which can be very difficult to achieve from a rational design perspective.[7] By maintaining the structure defined in the Capture SELEX process, our approach reduces the subsequent difficulty of engineering an optical switch, and the use of a fluorescent readout lets us rapidly screen many constructs in parallel using a plate reader. That being said, we would like to note that the DBS design could be applied to electrochemical detection as well, which could broaden the availability of aptamers that can be incorporated into electrochemical sensors.[47–49] In sum, the present work demonstrates the feasibility of using optical biosensing to achieve real-time detection of diverse biomarkers in complex samples via evanescent field-based sensing—an approach that until now has been limited to single-point measurements.[32]

4. Experimental Section

Reagents: All chemicals were purchased from Thermo Fisher Scientific unless otherwise noted. Oligonucleotides modified with Cy3, Iowa Black, or BHQ-2 were purified by HPLC and purchased from Integrated DNA Technologies. All sequences used in this work are shown in Table S1 (Supporting Information). All oligonucleotides were resuspended in nuclease-free water and stored at −20 °C. All experiments were performed in triplicate unless otherwise noted.

Measurement of Effective Binding Affinity: DBS constructs of varying L_{bubble} and L_{DS} were suspended at a concentration of 250×10^{-9} M in binding buffer (1× PBS, pH 7.5 and 2×10^{-3} M $MgCl_2$). Switches were prepared by mixing 1×10^{-6} M Cy3-labeled aptamer strand with 2×10^{-6} M quencher-coupled strand, heating to 95 °C, and then cooling to 25 °C over the course of 25 min to achieve hybridization. To obtain binding curves in solution, 40 µL reactions were prepared in binding buffer with 250×10^{-9} M DBS and final target concentrations in the range of 1×10^{-6} to 1×10^{-3} M for dopamine and 500×10^{-9} to 175×10^{-6} M for cortisol. Stock solutions of 20×10^{-3} M dopamine were prepared in 1.5 mL of binding buffer and 30×10^{-3} M cortisol in 1.5 mL of 100% ethanol. The fluorescence spectra for all samples were measured at 25 °C on a Synergy H1 microplate reader (BioTeK). Emission spectra were monitored in the 550–700 nm range with Cy3 excitation at 530 nm and a gain of 100 in Corning 96-well half area black flat-bottom polystyrene microplates. Representative concentration-dependent emission spectra are shown in Figure S1 (Supporting Information).

K_D^{eff} was extracted from triplicate data by fitting to the single-site specific binding equation in terms of relative fluorescence units (RFU) using GraphPad Prism (Table S2, Supporting Information).

$$y = (B_{max} - Y_{min})\frac{x}{x + K_D^{eff}} + Y_{min} \quad (1)$$

For ease of comparison, normalized data are presented in Figure 2. RFU data were first averaged to obtain a mean RFU per concentration point. Averaged data were then normalized as follows, where F_{min} is the minimum mean value and F_{max} is the maximum mean value.

$$F_{norm} = \frac{F - F_{min}}{F_{max} - F_{min}} \quad (2)$$

Measurement of Binding Kinetics: DBS constructs of varying L_{bubble} and L_{DS} were suspended at a concentration of 333.3×10^{-9} M in 30 µL of binding buffer. The switches were prepared as described above. Kinetic fluorescence measurements were made using a Synergy H1 microplate reader. After timed injection of 10 µL of 50×10^{-6} M dopamine in binding buffer into the 30 µL DBS solution, the kinetic response was measured. Cy3 was excited at 530 nm, and emission was measured at 570 nm using monochromators at the minimum possible regular time interval of 0.465 s. All kinetic data were normalized relative to the target-free control to account for the effect of sample volume change upon injection of dopamine. For plotting, the curves were normalized to a range of 0–1 in order to visually emphasize changes in rate constants rather than the background and peak levels that were dictated by the thermodynamics. These data were normalized as described above. Each replicate was normalized independently, and the normalized datasets were then averaged. The association time constant (τ) was obtained by fitting the data to the one-phase association curve using GraphPad Prism (Table S3, Supporting Information).

Slide Preparation for TIRF Microscopy: A detailed version of the coverslip cleaning procedure can be found in the Supporting Information of ref. [26]. Briefly, coverslips (25 mm × 25 mm × 170 µm) were soaked in piranha solution (25% H_2O_2 and 75% concentrated H_2SO_4) and sonicated for 90 min, followed by five rinses with Milli-Q water. The coverslips were then soaked with 0.5 M NaOH and sonicated for 30 min, followed by five more rinses with water. The slides were then soaked five times in HPLC-grade acetone with 5 min sonication in the fourth soak. Slides were then dried with N_2.

To prevent nonspecific adsorption of biomolecules onto the glass surface, the coverslips were functionalized prior to use with poly(ethylene glycol) silane (mPEG-sil, MW = 5000, Laysan Bio). For sample immobilization, a 99:1 ratio w/w of PEG-sil/biotin-PEG-sil was used. The coverslip was incubated with a 25% (w/w) mixture of PEG-sil/biotin-PEG-sil in DMSO (anhydrous) at 90 °C for 15 min. The excess PEG was rinsed off the coverslip with water (molecular biology grade), and the coverslips were dried under an N_2 stream. Imaging chambers (≈8 µL, 10 mm × 20 mm × 0.25 mm) were constructed by pressing a polycarbonate film with an adhesive gasket (Grace Bio labs) onto the PEG-coated coverslip. Before image acquisition, and to further decrease the level of non-specific binding, the surface was incubated for 10 min with 12 µL of passivation buffer (1× PBS, pH 7.5 and 1% v/v Tween 20). Next, the surface was incubated with 12 µL of 0.2 mg mL^{-1} (≈200×10^{-9} M, 1× PBS, pH 7.5) streptavidin solution for 10 min. The unbound streptavidin was washed away twice with 50 µL of 1× PBS buffer pH 7.5. For surface attachment, the displacement strand was conjugated at its 3′ end to a biotin moiety and at its 5′ end to an Iowa Black quencher, whereas the aptamer complement was internally modified with a Cy3 reporter. The DBS switch was prepared by mixing the Cy3-labeled aptamer strand with the biotinylated, quencher-coupled strand at a scale of 100×10^{-9} M and 150×10^{-9} M, respectively. This mixture was heated to 95 °C and then cooled to 25 °C over the course of 30 min to achieve hybridization. The construct was then immobilized onto the passivated, streptavidin-coated coverslip surface by incubating a 50×10^{-12} M solution of DBS in 1× binding buffer for 5 min followed by two washes of 50 µL of binding buffer. For long term imaging, 40 nanometer biotin-functionalized gold nanoparticles (Alfa Aesar/Thermo Scientific Chemicals, J67026AMI) were used as fiducial markers to facilitate drift correction. All experiments were conducted at room temperature.

TIRF Microscopy and Image Analysis: Fluorescence imaging was carried out using an inverted Nikon Eclipse Ti2 microscope equipped with the perfect focus system and implementing an objective-type TIRF configuration with a motorized Nikon TIRF illuminator (LAPP) and an oil-immersion objective (CFI Apo TIRF 60× oil immersion objective lens, numerical aperture 1.49). The effective pixel size was 180 nm. With these settings, a 532-nm laser was used for excitation (LUN-F XL 532/561/640 Laser Combiner; 3 mW, measured out of the objective). For Cy3 imaging, the laser beam was passed through a multiband cleanup filter (ZET532/640×, Chroma Technology) and coupled into the microscope objective using a multiband beam splitter (ZT532/640rpc-uf2, Chroma Technology). Fluorescence light was spectrally filtered with a ZET532/640m-trf (Chroma Technology) filter. Fluorescence was further filtered with an ET585/65m (Chroma Technology) emission filter mounted on a Ti2-P-FWB-E motorized barrier filter wheel. All movies were recorded onto a 704 × 704 pixel region of a back-illuminated Scientific CMOS camera (Prime 95B, 1.44 MP, Teledyne Photometrics). The camera and microscope were controlled using the NIS-Elements Advanced Research software package. Images were analyzed by creating a square ROI in the center of the image (512 × 512 pixels). We observed typically ≈400-800 spots over a field of view (≈92^2 um^2). Fluorescence intensity–time trajectories of individual molecules were extracted from the videos using a custom algorithm written in MATLAB (MathWorks) defining a diamond shaped region around the center of each spot captured. A surrounded region was defined to substract the local intensity background.

Fiber Probe Selection and Construction: Single- and multimode fibers are commercially available and have low attenuation (i.e., ≈3–5 dB km^{-1} at wavelengths of 650–850 nm, which is the bandwidth at which Cy3 emits). Background fluorescence was also a consideration; this is likely to originate from impurities in the fiber (color centers) and can dominate the spectrum in a poorly chosen fiber. To minimize this background emission, different types of fibers, including a) single- and multimode fibers, b) multimode fibers with different core diameters (100, 62.5, or 50 µm), c) multimode fibers with step index and graded index, and d) multimode fibers with high and low OH content, were screened. Figure S9 (Supporting Information) shows representative transmission spectra for different multimode fibers excited at 405/530/630 nm using appropriate laser lines with band- and long-pass filters in the excitation and detection paths. To minimize ambient light coupling to the fiber, which introduces background

signal offset, and to prevent damage to the fiber, reinforced tubing was used (Thorlabs FT038-BK) for multimode fibers. The background was lowest when using a graded index multimode fiber (Thorlabs GIF625) with a core diameter of 62.5 µm, cladding diameter of 125 µm, and an operating wavelength longer than 550 nm. Since the residual background counts from the fiber are constant, they can be easily subtracted from the measured signal to obtain the Cy3 signal.

Optical fibers confine light in a high refractive index core via total internal reflection, and a radially decaying evanescent field exists in the surrounding medium of lower refractive index. Tapering a fiber to the proper range of core diameter allows for the enhancement of the evanescent field in this region, thereby increasing the light coupled to the aptamer switches grafted on the surface of the taper. This in turn increases the sensing area compared to a fiber sensor with a cleaved end, where coupling can only occur at the fiber core. Evanescent coupling along the fiber taper has the added benefit of rejecting background signal from autofluorescence in biological settings (Figure S7, Supporting Information). In order to finely control fiber geometry and reproducibly fabricate high-performing fibers, a previously established heat-and-pull-based tapering protocol was adapted.[26] Several inches of plastic coating were stripped from a central section of the fiber before it was tapered using a Vytran GPX3000, using a custom recipe that produced ≈10-µm fiber waists, with intended up- and down-taper lengths of 10 mm. The taper parameters (i.e., up- and down-taper length and waist diameter) were chosen to produce the best compromise between requirements, namely, 1) maximizing the evanescent excitation of the fluorophores, 2) maximizing the selective collection of fluorophore emissions by the fiber core, and 3) reducing nonadiabatic scattering losses. After tapering, the two fiber ends were gently pulled mechanically using the microstage in order to cleave the tapered fiber at its waist and obtain two different fiber probes. Fiber tapering and cleavage consistently resulted in two visually distinct profiles (one on either side of the filament) with different taper lengths, referred to as "short" and "long" tapers. Although both tapers were usable, under the same conditions, long tapers generally produced about twice the signal as short tapers and were therefore used throughout the main text (Figure S10, Supporting Information). The tapering process yielded reproducible results, and while tapers can break, these were found to be mechanically strong enough to not be prohibitively sensitive during the measurements. It was recognized that specialized fiber-tapering systems might not be available in all labs; therefore, commercially available fiber optics were tested from companies such as LaseOptics as an alternative, and it was found that these provide comparable performance. In addition, more cost-effective approaches such as hydrofluoric acid etching for fabricating the taper are available and well-documented in the literature.[50,51]

Preparation of the Fiber Tips: A custom-built microstage setup was used to fine-tune the functionalized region of the fiber and consistently achieve a reproducible probe coating. The surfaces of the fiber tips were first cleaned and hydroxyl-activated by immersing them in piranha solution for 2 h, followed by a 10 min incubation/wash with ultrapure water, followed by acetone for 5 min. For the amination of the optical fiber, the probes were then kept for 5 min in 1% (v/v) Vectabond/acetone, washed with ultrapure water, and dried for 5 min at room temperature. In order to prevent nonspecific adsorption of biomolecules onto the glass surface, these surface-attached amine groups were incubated with a mixture of poly(ethylene glycol) succinimidyl valerate (mPEG-SVA, MW = 5000) and biotin-PEG-SVA at a ratio of 90:10 (w/w) in 110×10^{-3} M sodium bicarbonate for 3 h and then rinsed with water and left in a dried state until used.

A polycarbonate chamber (≈40 µL, Grace Bio labs HybriWell Sealing systems) was then constructed on the probe tip by pressing a polycarbonate film with an adhesive gasket onto the coated fiber in order to surround the probe (Figure S8, Supporting Information). Two silicone connectors were glued onto the predrilled holes of the film and served as inlet and outlet ports to manually dispense/wash different solutions into the chamber. Before data acquisition, the chamber was filled with 40 µL of 0.2 mg mL^{-1} ($\approx 200 \times 10^{-9}$ M) neutravidin solution for 10 min. The unbound neutravidin was washed away twice with 200 µL of 1× buffer (1× PBS, pH 7.5 and 2×10^{-3} M $MgCl_2$). Biotinylated Cy3- and quencher-modified DBS constructs were then prepared as described above and immobilized onto the passivated, neutravidin-coated fiber surface by incubating the chamber for 1 h with 40 µL of 250×10^{-9} M DBS solution in 1× binding buffer followed by washing with more binding buffer. All experiments were conducted at room temperature. In the control experiments, the PEGylated fiber sensor was incubated with 40 µL of 250×10^{-9} M Cy3-labeled DNA solution in 1× binding buffer in the absence of neutravidin. Measurements were taken with the Cy3-labeled DNA still in solution (solution signal) and after washing the fiber with 1× binding buffer (nonspecific binding signal). These measurements were compared to the specific signal after incubating the PEGylated fiber sensor with neutravidin, washing, incubating with 250×10^{-9} M Cy3-labeled DNA, and washing (as described above). Minimal signal in this control experiment was observed, confirming that 1) there is minimal nonspecific binding of aptamer switches to the sensor surface, and 2) the fiber operates as a near-field sensor and only detects signals close to the surface, with minimal interference from fluorophores in solution (Figure S7, Supporting Information).

Preparation of Target Solutions for Real-Time Measurements: For the dopamine experiments, a stock of 20×10^{-3} M dopamine was prepared in 1.5 mL of binding buffer or aCSF (124×10^{-3} M NaCl, 2.5×10^{-3} M KCl, 10×10^{-3} M glucose, 26×10^{-3} M $NaHCO_3$, 1×10^{-3} M NaH_2PO_4, 2.5×10^{-3} M $CaCl_2$, and 1.3×10^{-3} M $MgSO_4$).[52] Serial dilutions were then performed to prepare solutions of 0, 200×10^{-9}, 500×10^{-9}, 1×10^{-6}, 5×10^{-6}, 8×10^{-6}, 15×10^{-6}, 20×10^{-6}, 80×10^{-6}, 200×10^{-6}, or 800×10^{-6} M dopamine in buffer or aCSF. Due to the propensity of dopamine to form polydopamine at higher concentrations, the dopamine stock had to be renewed every ≈30 min during the experiment to ensure minimal precipitation on the probe surface or fouling of aptamer structures. This change in stocks resulted in slight variation in the measured signal, which was more noticeable in the aCSF due to its faster reaction rate.[53]

For cortisol experiments, since cortisol is poorly soluble in aqueous conditions, a stock solution of 30×10^{-3} M cortisol was first prepared in 1.5 mL of 100% ethanol. A serial dilution was then done in binding buffer to prepare solutions of 50×10^{-9}, 200×10^{-9}, 500×10^{-9}, 1×10^{-6}, 1.4×10^{-6}, 10×10^{-6}, 50×10^{-6}, 100×10^{-6}, and 140×10^{-6} M cortisol. Different solutions were subsequently injected into the sample chamber, exchanging solutions at a 1-min interval while continuously recording. For experiments with human plasma, the cortisol stock was used in 100% ethanol to prepare serial dilutions in human plasma at 99.5% final plasma concentration (50×10^{-9}, 200×10^{-9}, 500×10^{-9}, 1×10^{-6}, 1.4×10^{-6}, 50×10^{-6}, and 140×10^{-6} M). It is important to note that the dilutions for each sample were freshly prepared right before measurements because cortisol-binding proteins in the plasma samples contributed to discrepancies in measurements when older, preprepared samples were used. Source data for all concentrations tested are provided as a Source Data file.

Optoelectronic System Setup for Real-Time Measurements: Fluorescence detection was carried out using a SPCM, which utilizes single-photon avalanche diodes, and can therefore achieve high quantum efficiency and low noise characteristics. Their high sensitivity and low background noise, coupled with the quenched DBS design, made it possible to detect analytes at concentrations considerably lower than the aptamer K_D.[54] The detector was interfaced to a custom-designed acquisition board based on an Arduino to process and analyze detected photons, record detection events, and monitor fluorescence intensity over time. Data acquisition was performed with a LabVIEW GUI with an integration time of 500 ms. For excitation, a fiber-coupled 532 nm laser was used (Coherent, 20 mW, measured out of the fiber). For Cy3 measurements, the laser beam was passed through a band-pass cleanup filter (532/10, Chroma Technology) and variable neutral density filter (Thorlabs NDC-50C-4M) and coupled into the sample fiber using a fiber coupler (62.5/125 µm multimode fiber coupler 90/10, FC/PC, Thorlabs) and fiber switch (Newport MPSN-62-12-FCPC) using the appropriate optics and mounts (In-Line Fiber Optic Filter Mount, FC/PC, Thorlabs). The fiber switch modulated the on/off state of the laser beam, allowing the precise control of the duration and timing of the laser pulse for continuous and intermittent measurements. Fluorescence emission light from the fiber sample was collected back through a fiber coupler (62.5/125 µm multimode fiber coupler 50/50, FC/PC, Thorlabs) and spectrally filtered with

band-pass filters (595/50, Chroma Technology; 676/29, Semrock). Aligning the fluorescence emission signal with the SPCM using lenses (Ø8 mm achromatic doublet, threaded mount, Thorlabs) and mirrors is critical to ensure that the incident light is focused, well-centered, and collimated on the active area of the detector, allowing the highest detection efficiency while rejecting other background light. An image of the hardware system and detailed assembly instructions are included in Note S2 (Supporting Information).

Data collected from the SPCM were analyzed in MATLAB. Background signal was measured for each fiber probe (laser power at 500 nW, no DBS on the probe surface) and averaged to calculate a background value per fiber. Data were first segmented into sections of different concentrations either by finding the edges of regions of 0 s (for intermittent data with SPCM turned OFF between measurements) or manually (for continuous data). The signal per concentration section was calculated in order to extract a binding curve. If the signal increased or decreased by more than 5% over the section, the data were fitted to an exponential gain or decay, and the plateau value was reported. If the signal decreased by more than 15% over the section, the data were fitted to an exponential decay, and the plateau value was reported. The exponential rate was also returned and used to characterize kinetics of the DBS constructs on fiber. Otherwise, the average value over the section was calculated. The background value of the fiber was subtracted from all calculated signals. Baseline values were defined as the average background-corrected signal over times when no target was present. Signal gain values reported in binding curves were calculated by normalizing the background-corrected signals to the average of the nearest baseline sections prior to and after the concentration was measured. Real-time data were normalized to the average baseline value over the entire data file. Signal gain values reported in Figure 5b were normalized to the average baseline within the five (or ten) cycle measurements. In these experiments, LODs were defined as the lowest experimentally measured concentration for which the average signal gain from triplicate experiments was significantly different from the average background signal gain values in the adjacent baseline segments that preceded sample addition ($p < 0.05$ on an unpaired t-test).

Supporting Information

Supporting Information is available from the Wiley Online Library or from the author.

Acknowledgements

The authors would like to acknowledge the contribution of Michael Silvernagel, Xiaoyuan (Sandra) Hu, Peter Mage, Dong-Wook Park, Anping Li, Alex Codik, Kang Yong Loh, Brandon Wilson, Alexandra Rangel, Sharon Newman, Dries Vercruysse and all current members of the Soh lab for their important help throughout the project. The authors would also like to acknowledge the contributions of members of the Malenka lab, including Wade K. Morishita, Daniel Cardozo Pinto, Mathew B. Pomrenze, Paul Holbert, and Prof. Robert Malenka, who provided valuable insights, productive discussions, and experimental help throughout the course of the work. The authors would also like to thank SNF and SNSF for providing access to cleanroom and SEM facilities. H.T.S. would like to acknowledge support from the Helmsley Trust, Wellcome LEAP SAVE program, and the National Institutes of Health (NIH, OT2OD025342). A.A.H. acknowledges support from the Sanjiv Sam Gambhir—Philips Fellowship Program in Precision Health and the NSERC Postdoctoral Fellowships (PDF, Canada). C.D. acknowledges support from the Andreas Bechtolsheim Stanford Graduate Fellowship and the Microsoft Research Ph.D. Fellowship. A.P.C. acknowledges support from the NSF Graduate Research Fellowship Program and the Stanford Graduate Fellowship. S.Y. acknowledges support from the Stanford Graduate Fellowship program. I.A.P.T. acknowledges the support of the Medtronic Foundation Stanford Graduate Fellowship and the Natural Sciences and Engineering Research Council of Canada (NSERC).

Conflict of Interest

The authors declare no conflict of interest.

Author Contributions

A.A.H., A.P.C., and C.D. contributed equally to this work. H.T.S., J.V., A.A.H., C.D., and A.P.C. conceived the initial concept. A.A.H., C.D., and A.P.C. designed the experiments. A.A.H. designed and optimized the DBS construct. A.A.H., A.P.C., K. X. F., D.W., and T.F. conducted troubleshooting of aptamer switch designs. B.E.Y. synthesized quencher-labeled DNA. A.A.H. and A.P.C. executed the solution-based experiments. C.D. and A.P.C. designed/fabricated/aligned the optoelectronic system. N.M. designed and fabricated the Arduino board. A.A.H., A.P.C., C.D., and S.Y. executed the fiber-based experiments. C.D. and A.P.C. developed the software and analyzed the fiber-based data. Y.G. designed and executed the single-molecule experiments and analyzed the corresponding data. A.P.C., K.Y., I.A.P.T., B.H.A., and M.J. F. D. designed the fiber-tapering protocol. A.P.C. optimized and executed the fiber-tapering protocol. A.A.H., A.P.C., M.E., and H.T.S. wrote the manuscript. All authors edited, discussed, and approved the whole paper.

Data Availability Statement

The data that support the findings of this study are available from the corresponding author upon reasonable request.

Keywords

aptamer switches, biomedical probes, biosensor, functional materials, real-time detection

Received: May 10, 2023
Revised: November 10, 2023
Published online:

[1] B. S. Ferguson, D. A. Hoggarth, D. Maliniak, K. Ploense, R. J. White, N. Woodward, K. Hsieh, A. J. Bonham, M. Eisenstein, T. E. Kippin, K. W. Plaxco, H. T. Soh, *Sci. Transl. Med.* **2013**, *5*, 213ra165.
[2] K. W. Plaxco, H. T. Soh, *Trends Biotechnol.* **2011**, *29*, 1.
[3] A. E. Rangel, A. A. Hariri, M. Eisenstein, H. T. Soh, *Adv. Mater.* **2020**, *32*, 2003704.
[4] N. Hamaguchi, A. Ellington, M. Stanton, *Anal. Biochem.* **2001**, *294*, 126.
[5] A. A. Sanford, A. E. Rangel, T. A. Feagin, R. G. Lowery, H. S. Argueta-Gonzalez, J. M. Heemstra, *Chem. Sci.* **2021**, *12*, 11692.
[6] N. Arroyo-Currás, J. Somerson, P. A. Vieira, K. L. Ploense, T. E. Kippin, K. W. Plaxco, *Proc. Natl. Acad. Sci. USA* **2017**, *114*, 645.
[7] A. M. Downs, K. W. Plaxco, *ACS Sens.* **2022**, *7*, 2823.
[8] P. L. Mage, B. S. Ferguson, D. Maliniak, K. L. Ploense, T. E. Kippin, H. T. Soh, *Nat. Biomed. Eng.* **2017**, *1*, 0070.
[9] S. Li, L. Lin, X. Chang, Z. Si, K. W. Plaxco, M. Khine, H. Li, F. Xia, *RSC Adv.* **2021**, *11*, 671.
[10] M. Santos-Cancel, L. W. Simpson, J. B. Leach, R. J. White, *ACS Chem. Neurosci.* **2019**, *10*, 2070.
[11] Y. Xiao, T. Uzawa, R. J. White, D. Demartini, K. W. Plaxco, *Electroanalysis* **2009**, *21*, 1267.
[12] J. D. Munzar, A. Ng, M. Corrado, D. Juncker, *Chem. Sci.* **2017**, *8*, 2251.
[13] R. Nutiu, Y. Li, *J. Am. Chem. Soc.* **2003**, *125*, 4771.
[14] K.-A. Yang, H. Chun, Y. Zhang, S. Pecic, N. Nakatsuka, A. M. Andrews, T. S. Worgall, M. N. Stojanovic, *ACS Chem. Biol.* **2017**, *12*, 3103.

[15] T. A. Feagin, N. Maganzini, H. T. Soh, *ACS Sens.* **2018**, *3*, 1611.
[16] Z. Tang, P. Mallikaratchy, R. Yang, Y. Kim, Z. Zhu, H. Wang, W. Tan, *J. Am. Chem. Soc.* **2008**, *130*, 11268.
[17] J. J. Li, X. Fang, W. Tan, *Biochem. Biophys. Res. Commun.* **2002**, *292*, 31.
[18] B. D. Wilson, A. A. Hariri, I. A. P. Thompson, M. Eisenstein, H. T. Soh, *Nat. Commun.* **2019**, *10*, 5079.
[19] M. N. Stojanovic, P. De Prada, D. W. Landry, *J. Am. Chem. Soc.* **2001**, *123*, 4928.
[20] A. Vallée-Bélisle, K. W. Plaxco, *Curr. Opin. Struct. Biol.* **2010**, *20*, 518.
[21] R. Stoltenburg, N. Nikolaus, B. Strehlitz, *J. Anal. Methods Chem*. **2012**, *2012*, 415697.
[22] C. Niu, C. Zhang, J. Liu, *Environ. Sci. Technol.* **2022**, *56*, 17702.
[23] N. Nakatsuka, K.-A. Yang, J. M. Abendroth, K. M. Cheung, X. Xu, H. Yang, C. Zhao, B. Zhu, Y. S. Rim, Y. Yang, P. S. Weiss, M. N. Stojanovic, A. M. Andrews, *Science* **2018**, *362*, 319.
[24] K.-A. Yang, R. Pei, D. Stefanovic, M. N. Stojanovic, *J. Am. Chem. Soc.* **2012**, *134*, 1642.
[25] S. Xu, J. Zhan, B. Man, S. Jiang, W. Yue, S. Gao, C. Guo, H. Liu, Z. Li, J. Wang, Y. Zhou, *Nat. Commun.* **2017**, *8*, 14902.
[26] Y. Gidi, S. Bayram, C. J. Ablenas, A. S. Blum, G. Cosa, *ACS Appl. Mater. Interfaces* **2018**, *10*, 39505.
[27] C. Daniel, Y. Roupioz, D. Gasparutto, T. Livache, A. Buhot, *PLoS One* **2013**, *8*, 75419.
[28] A. A. Hariri, S. S. Newman, S. Tan, D. Mamerow, A. M. Adams, N. Maganzini, B. L. Zhong, M. Eiseinstein, A. R. Dunn, H. T. Soh, *Nat. Commun.* **2022**, *13*, 5359.
[29] C. S. Huertas, O. Calvo-Lozano, A. Mitchell, L. M. Lechuga, *Front. Chem.* **2019**, *7*, 724.
[30] M. Loyez, M. C. DeRosa, C. Caucheteur, R. Wattiez, *Biosens. Bioelectron.* **2022**, *196*, 113694.
[31] S. Tierney, B. M. H. Falch, D. R. Hjelme, B. T. Stokke, *Anal. Chem.* **2009**, *81*, 3630.
[32] Y. Tang, F. Long, C. Gu, C. Wang, S. Han, M. He, *Anal. Chim. Acta* **2016**, *933*, 182.
[33] M. L. A. V. Heien, A. S. Khan, J. L. Ariansen, J. F. Cheer, P. E. M. Phillips, K. M. Wassum, R. M. Wightman, *Proc. Natl. Acad. Sci. USA* **2005**, *102*, 10023.
[34] X. Liu, J. Liu, *VIEW* **2021**, *2*, 20200102.
[35] J. G. Roberts, L. Z. Lugo-Morales, P. L. Loziuk, L. A. Sombers, *Methods Mol. Biol.* **2013**, *964*, 275.
[36] J.-S. Raul, V. Cirimele, B. Ludes, P. Kintz, *Clin. Biochem.* **2004**, *37*, 1105.
[37] J. E. An, K. H. Kim, S. J. Park, S. E. Seo, J. Kim, S. Ha, J. Bae, O. S. Kwon, *ACS Sens.* **2022**, *7*, 99.
[38] J. G. Lewis, C. J. Bagley, P. A. Elder, A. W. Bachmann, D. J. Torpy, *Clin. Chim. Acta* **2005**, *359*, 189.
[39] R. C. Bhake, V. Kluckner, H. Stassen, G. M. Russell, J. Leendertz, K. Stevens, A. C. E. Linthorst, S. L. Lightman, *J. Clin. Endocrinol. Metab.* **2019**, *104*, 5935.
[40] M. Kadmiel, J. A. Cidlowski, *Trends Pharmacol. Sci.* **2013**, *34*, 518.
[41] L. Van Smeden, A. Saris, K. Sergelen, A. M. De Jong, J. Yan, M. W. J. Prins, *ACS Sens.* **2022**, *7*, 3041.
[42] D. Wu, T. Feagin, P. Mage, A. Rangel, L. Wan, D. Kong, A. Li, J. Coller, M. Eisenstein, H. Soh, *Anal. Chem.* **2023**, *95*, 2645.
[43] D. Wu, C. K. L. Gordon, J. H. Shin, M. Eisenstein, H. T. Soh, *Acc. Chem. Res.* **2022**, *55*, 685.
[44] A. François, T. Reynolds, N. Riesen, J. M. M. Hall, M. R. Henderson, E. Zhao, S. Afshar, T. M. Monro, *MRS Adv.* **2016**, *1*, 2309.
[45] A. M. Downs, J. Gerson, K. K. Leung, K. M. Honeywell, T. Kippin, K. W. Plaxco, *Sci. Rep.* **2022**, *12*, 5535.
[46] A. Shaver, N. Kundu, B. E. Young, P. A. Vieira, J. T. Sczepanski, N. Arroyo-Currás, *Langmuir* **2021**, *37*, 5213.
[47] M. Labib, E. H. Sargent, S. O. Kelley, *Chem. Rev.* **2016**, *116*, 9001.
[48] A. Idili, J. Gerson, T. Kippin, K. W. Plaxco, *Anal. Chem.* **2021**, *93*, 4023.
[49] P. Dauphin-Ducharme, K. Yang, N. Arroyo-Currás, K. L. Ploense, Y. Zhang, J. Gerson, M. Kurnik, T. E. Kippin, M. N. Stojanovic, K. W. Plaxco, *ACS Sens.* **2019**, *4*, 2832.
[50] P. Zaca-Morán, J. P. Padilla-Martínez, J. M. Pérez-Corte, J. A. Dávila-Pintle, J. G. Ortega-Mendoza, N. Morales, *Laser Phys.* **2018**, *28*, 116002.
[51] Y.-H. Lai, K. Y. Yang, M.-G. Suh, K. J. Vahala, *Opt. Express* **2017**, *25*, 22312.
[52] B. D. Heifets, J. S. Salgado, M. D. Taylor, P. Hoerbelt, D. F. Cardozo Pinto, E. E. Steinberg, J. J. Walsh, J. Y. Sze, R. C. Malenka, *Sci. Transl. Med.* **2019**, *11*, 522.
[53] M. Alfieri, L. Panzella, S. Oscurato, M. Salvatore, R. Avolio, M. Errico, P. Maddalena, A. Napolitano, M. D'ischia, *Biomimetics* **2018**, *3*, 26.
[54] B. D. Wilson, H. T. Soh, *Trends Biochem. Sci.* **2020**, *45*, 639.
[55] G. Bonnet, O. Krichevsky, A. Libchaber, *Proc. Natl. Acad. Sci. USA* **1998**, *95*, 8602.
[56] A. D. Vogt, E. Di Cera, *Biochemistry* **2012**, *51*, 5894.